Large eddy simulation of wind turbine wake dynamics in the stable boundary layer using the Weather Research and Forecasting Model

Matthew L. Aitken,[1,a)] Branko Kosović,[2)] Jeffrey D. Mirocha,[3)] and Julie K. Lundquist[4,5)]

[1]*Department of Physics, University of Colorado, 390 UCB, Boulder, Colorado, 80309-0390, USA*

[2]*National Center for Atmospheric Research, P.O. Box 3000, Boulder, Colorado, 80307, USA*

[3]*Lawrence Livermore National Laboratory, 7000 East Avenue, Livermore, California, 94551, USA*

[4]*Department of Atmospheric and Oceanic Sciences, University of Colorado, 311 UCB, Boulder, Colorado, 80309-0311 USA*

[5]*National Renewable Energy Laboratory, 15013 Denver West Parkway, Golden, Colorado, 80401-3305, USA*

Recently, an actuator disk parameterization was implemented in the Weather Research and Forecasting (WRF) Model for large eddy simulation (LES) of wind turbine wakes. To thoroughly verify this model, simulations of various types of turbines and atmospheric conditions must be evaluated against corresponding experimental data. In this work, numerical simulations are compared to nacelle-based scanning lidar measurements taken in stable atmospheric conditions during a field campaign conducted at a wind farm in the western United States. Using several wake characteristics—such as the velocity deficit, centerline location, and wake width—as metrics for model verification, the simulations show good agreement with the observations. Notable results include a high average velocity deficit, decreasing from 73% at a downwind distance x of 1.2 rotor diameters (D) to 25% at x = 6.6D, resulting from a low average wind speed and therefore high average turbine thrust coefficient. Moreover, the wake width expands from 1.4D at x = 1.2D to 2.3D at x = 6.6D. Finally, new features—namely rotor tilt and drag from the nacelle and tower—are added to the existing actuator disk model in WRF-LES. Compared to the rotor, the effect of the tower and nacelle on the flow is relatively small but nevertheless important for an accurate representation of the entire turbine. Adding rotor tilt to the model causes the vertical location of the wake center to shift upward. Continued advancement of the actuator disk model in WRF-LES will help lead to optimized turbine siting and controls at wind farms.

[a)] Electronic mail: matthew.aitken@colorado.edu

I. INTRODUCTION

At utility-scale wind farms, turbine power output and fatigue loading are determined by aerodynamic forces acting on the blades, which vary because of heterogeneity in the ambient flow and because of wakes produced by neighboring turbines. Although often capable of directly resolving large turbulence scales, computational fluid dynamics (CFD) models generally lack many of the important physical processes that influence turbulence dynamics, such as radiation transfer between the surface and the atmosphere, the formation and evolution of clouds, as well as vegetation and soil moisture, which can include snow cover and sea ice. In an effort to predict wind turbine wake behavior in realistic atmospheric boundary layers, a rotating actuator disk model (Mirocha et al. 2014) was recently implemented in the large eddy simulation (LES) package within the Weather Research and Forecasting (WRF) Model (Skamarock et al. 2008), a numerical weather prediction system with a wide range of meteorological applications. The actuator disk method incorporates both the conservation of momentum and blade element theory—in which lift and drag are calculated at various sections of the blades—to describe the airflow through the rotor and the resulting wake behind the turbine. By representing the dynamics of the real atmosphere with higher fidelity than current industry standards, the turbine model in WRF-LES, once fully verified, should help to advance the simulations used in wind farm design and operation, leading to more efficient and cost-effective turbine layouts and controls.

The nature of the atmospheric boundary layer varies over a wide range of timescales, including, but not limited to, diurnal, seasonal, and annual cycles. While unstable conditions—typically occurring during the day—are often characterized by convective cells, stable conditions—typically occurring at night—frequently feature strong shear and intermittent turbulence associated with Kelvin-Helmholtz waves (Blumen et al. 2001; Mahrt 2014). Given the strong dependence of wind turbine performance on turbulence and stability (Kelley et al. 2006; Wagner et al. 2009; Barthelmie and Jensen 2010; Wharton

and Lundquist 2012; Churchfield et al. 2012; Hansen et al. 2012; Vanderwende and Lundquist 2012; Sathe et al. 2013), comprehensive verification of the actuator disk model in WRF-LES requires simulating a wide range of atmospheric conditions. Whereas Mirocha et al. (2014) evaluated simulations of a wind turbine wake against a subset of ground-based lidar measurements taken in convective conditions during the Turbine Wake and Inflow Characterization Study (Smalikho et al. 2013; Aitken et al. 2014), the present work compares simulations to nacelle-based lidar wake measurements of a different turbine operating in a stable boundary layer (SBL) during a separate field experiment described in Aitken and Lundquist (2014). Moreover, new features—namely, rotor tilt and drag from the nacelle and tower—are added to the existing actuator disk framework.

Of course, the SBL is important to study but also notoriously difficult to simulate (Mahrt 2014). The length scale of turbulent motions is relatively small in stable conditions, such that higher grid resolution is required in comparison to neutral and convective conditions. In LES, the effects of sub-filter scale (SFS) motions on the resolved scales are represented with a turbulence closure scheme, which must be selected carefully to sustain resolved turbulence. Coarse grid resolution and dissipative SFS models can cause boundary layer turbulence to collapse in SBL simulations, resulting in a false laminar flow field and runaway cooling at the surface. Because of the challenges involved, LES of the SBL has been mostly limited to idealized conditions with high geostrophic forcing or weak to moderate stability (Saiki et al. 2000; Kosović and Curry 2000; Basu and Porté-Agel 2006; Zhou and Chow 2011; Park et al. 2014). Here, we present a preliminary study of a wind turbine operating in an idealized SBL, to lay the groundwork for the addition of more realistic features—such as terrain and inflow conditions from parent mesoscale models—in future work.

In what follows, Section II provides an overview of both the experimental and computational methodology. Results and conclusions are presented in Sections III and IV, respectively.

II. DATA AND METHODS

A. Field experiment

Results from the large eddy simulation were compared to observations from a field experiment conducted in the fall of 2011 at a wind farm in the western United States, in which a Galion G4000 Lidar was used to measure wakes from the nacelle of a utility-scale wind turbine (Aitken and Lundquist 2014). With certain details about the experiment needing to remain confidential because of a nondisclosure agreement, the wind farm comprises turbines with rotor diameter $D \approx 100$ m and hub height $H \approx 80$ m, in addition to cut-in, rated, and cut-out speeds of about 4 m s^{-1}, 13 m s^{-1}, and 25 m s^{-1}, respectively. With strong winds typically channeled from the south-southwest, the wind farm is arranged in a series of rows spaced 15D along the prevailing wind direction (north-south) and 3D along the transverse direction (east-west), as seen in Fig. 1 of Aitken and Lundquist (2014).

During the experiment, wind speed and direction data were collected at hub height with a Risø P2546A cup anemometer (accuracy of 1% of reading) and Met One 020C wind vane (accuracy of 3°) mounted on an onsite meteorological (met) tower located in the southernmost row of turbines. In addition, atmospheric stability was determined using temperature measurements at 2 m and 76 m from another offsite met tower located approximately 12.4 km to the north of the onsite tower. Temperature was measured using Met One 083E-1-35 sensors to an accuracy of 0.1 K. Lidar measurements were taken during the period 14 September 2011 to 12 October 2011 from the turbine located just to the east of the onsite met tower, up to a maximum range of 4000 m and with a measurement accuracy of 0.1 m s^{-1}, depending on atmospheric conditions (Aitken et al. 2012). Plan position indicator (PPI) scans—in which the azimuth angle of the beam is swept while holding the elevation angle fixed—were used to sample the wake and surrounding flow field at discrete 60-m intervals. In each scan, the azimuth was swept through an angle of 84°—symmetric about the longitudinal axis of the turbine—with azimuthal

resolution $\Delta\theta = 3°$, while holding the elevation angle fixed at 0°. With the lidar beam held fixed for ~8 s at each azimuth angle, the scans lasted approximately 4 min each, which is long enough for meandering to influence estimation of the wake characteristics, as discussed in Aitken and Lundquist (2014).

B. Case study

The dataset was searched for periods lasting several hours and featuring quasi-steady flow conditions—i.e., nearly constant wind speed and direction—to allow representative averages of the wake parameters to be determined. One such interval occurred on 2 October 2011 between 02:30 and 07:30 local daylight time (LDT). Fig. 1 shows the wind speed and direction measured at hub height by the onsite tower, as well as the two temperature readings from the offsite tower, from this period. Note that the wind speed fluctuated between 4 and 8 m s^{-1} with an average value of 6.5 m s^{-1}, while the wind direction varied over a range of about 20 degrees. The time-of-day, temperature profile, and surface cooling are consistent with stable atmospheric conditions, and there was no cloud cover or precipitation according to National Weather Service records. Whereas temperature exhibited a decreasing trend with time, the lack of corresponding trends in the wind speed and direction suggests relatively constant large-scale forcing. An earlier study (Basu et al. 2008) suggested that the surface cooling rate—as opposed to the surface heat flux—should be prescribed as the lower boundary condition when simulating the stable boundary layer. When a line of best fit is applied to the 2-m temperature measurements (Fig. 1c), the slope indicates that the average cooling rate over the 5-hour period was about 0.2 K h^{-1}.

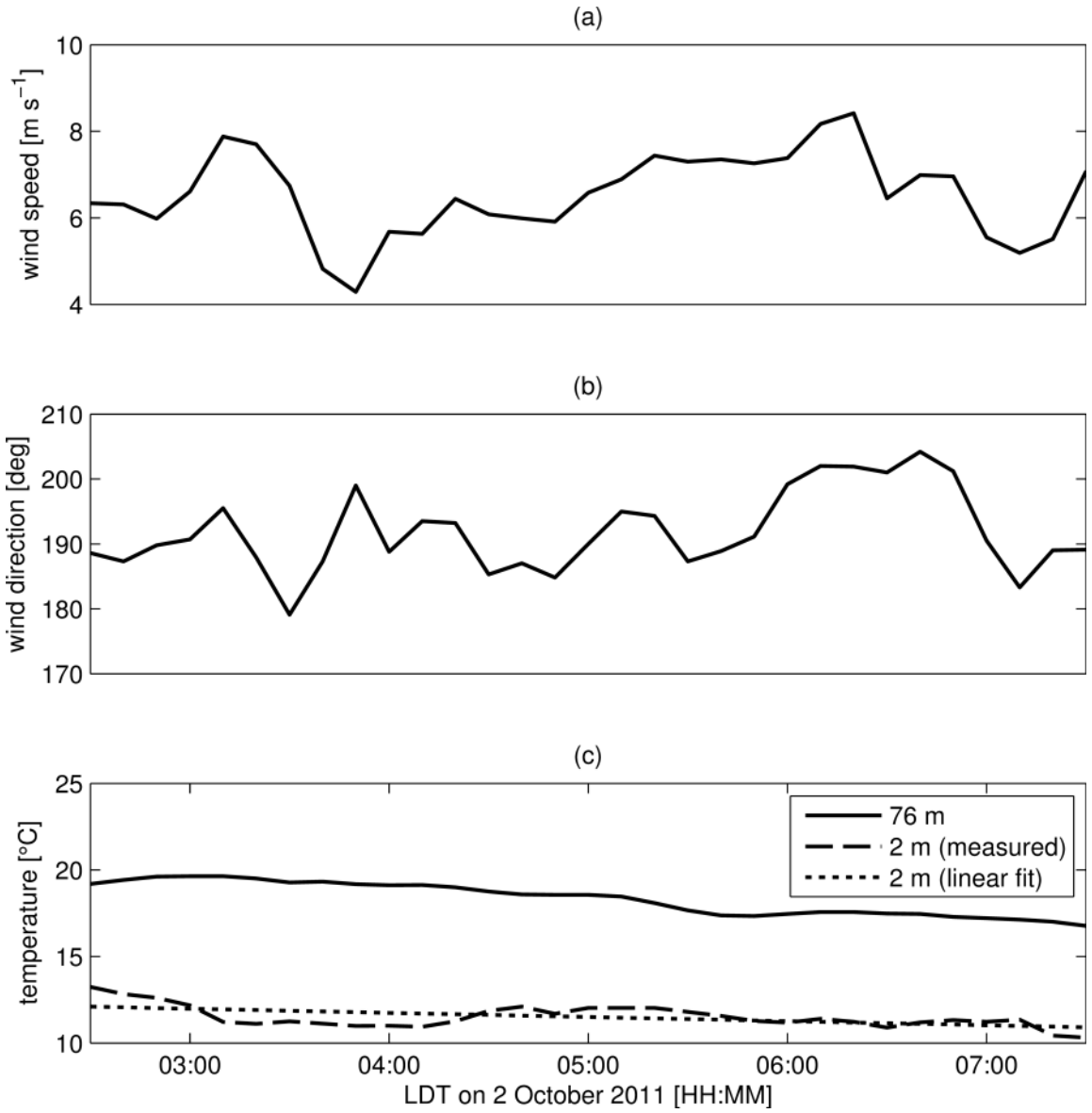

FIG. 1. (a) Wind speed and (b) direction measured at hub height by the onsite met tower during the case study period on 2 October 2011. (c) The offsite temperature reading at 76 m, as well as the 2-m temperature measurement and corresponding line of best fit.

C. Simulation setup

Following Mirocha et al. (2014), the simulation was carried out using the idealized LES framework within WRF, with a fine-scale inner domain (2400 m × 1000 m) nested one-way within a coarser outer domain (3600 m × 1500 m). Lateral grid spacing was set as $dx = dy = 15$ m on the outer domain and $dx = dy = 5$ m on the inner domain. The pressure-based vertical coordinate in WRF allows for an

approximate specification of the vertical mesh resolution dz, which was set to ~5 m up to a height of 200 m and then stretched by 5% per grid level up to the model top (~650 m) for both domains. The actuator disk was placed 7.5D (16.5D) from the inflow (outflow) boundary of the inner domain and centered in the transverse direction. The setup was designed to allow smaller turbulence structures consistent with the finer grid spacing to develop upstream of the turbine. Furthermore, with velocity deficits usually observed to be almost negligible once the wake is 10–12D downwind of the turbine (Vermeer et al. 2003; Smalikho et al. 2013), the entire wake ought to be contained within the inner domain, a fact confirmed upon examination of the WRF-LES output files.

The computational setup was simplified by orienting the predominant inflow direction at hub height to be parallel to the x-axis. A geostrophic wind with $u = 6.80$ m s^{-1} and $v = -3.17$ m s^{-1} was specified to yield an average wind speed at hub height approximately equal to the mean value of 6.5 m s^{-1} measured by the onsite met tower over the case study period. In addition, a uniform initial potential temperature profile was specified, with $\theta = 300$ K for $z < 150$ m and $d\theta/dz = 0.01$ K m^{-1} for $z > 150$ m, creating a capping inversion to prevent turbulence from reaching the model top. Random perturbations were imposed at the outset on the mean temperature field up to $z = 150$ m to initiate the turbulent motion.

The simulation was initialized dry with zero latent flux, and no cloud, radiation, or land surface models were specified. Surface boundary conditions were specified using Monin-Obukhov similarity theory, and the surface cooling rate was set uniformly in both space and time to the measured value of 0.2 K h^{-1} to simulate the stable conditions. A Rayleigh damping layer with a coefficient of 0.003 s^{-1} was applied to the upper 150 m of each domain to avoid spurious wave reflection from the model top. Because the Smagorinsky model is generally too dissipative for SBL simulations (Kosović and Curry 2000; Zhou and Chow 2011), the nonlinear backscatter anisotropy (NBA) model developed in Kosović (1997) and implemented in Mirocha et al. (2010) was chosen as the sub-grid scale closure scheme.

Periodic lateral boundary conditions were specified for the outer domain, which was run for 9 hours to spin-up turbulence consistent with the geostrophic wind and surface forcing. After starting the inner domain with the actuator disk at the beginning of hour 9, the simulation continued to run for another 5.5 hours. The first half hour of the inner domain solution was discarded, as spurious gravity waves may be initially present upon introduction of the inner domain. Instantaneous velocity fields were saved at an interval of 8 s, to correspond to the discretization of the measured lidar data.

D. Modifications to the actuator disk model in WRF-LES

Lookup tables for the blade characteristics and control schedule were changed in the actuator disk module to correspond to the turbine in Aitken and Lundquist (2014). In addition, the effects on the flow by the nacelle and tower were added to the existing wind turbine formulation. Namely, the nacelle is represented as a permeable disk normal to the inflow with radius R_{nac} and area $A_{\text{nac}} = \pi R_{\text{nac}}^2$. The drag force exerted by the nacelle on the flow is given by

$$F_{\text{nac}} = \frac{1}{2} C_{D,\text{nac}} \rho A_{\text{nac}} V_{\text{nac}}^2 , \tag{1}$$

where $C_{D,\text{nac}}$ is the drag coefficient of the nacelle, ρ is air density, and V_{nac} is the component of the incident wind velocity normal to the face of the nacelle. Following El Kasmi and Masson (2008), we set $C_{D,\text{nac}} = 1$. A similar approach is taken to model the effect of the tower, which has a cylindrical shape with radius R_{tower} and area $A_{\text{tower}} = 2R_{\text{tower}}H$ normal to the flow. The drag coefficient of the tower $C_{D,\text{tower}}$ is set to 1.2, after Wu and Porté-Agel (2011).

Additionally, the effect of rotor tilt was also added to the model, following the approach in Mikkelsen (2003). In blade element momentum (BEM) theory, the freestream wind speed V_0 used to calculate the lift and drag forces along the blades is taken to be the component of the flow normal to the rotor plane of rotation. Following the coordinate system convention in Mirocha et al. (2014)—cf. Fig.

2—the vector normal to the rotor plane amounts to a rotation of the unit vector $\hat{\boldsymbol{x}}'' = [1\ 0\ 0]^{\mathrm{T}}$ by the yaw angle Φ about the z''-axis:

$$\hat{\boldsymbol{x}}' = \begin{bmatrix} \cos\Phi & -\sin\Phi & 0 \\ \sin\Phi & \cos\Phi & 0 \\ 0 & 0 & 1 \end{bmatrix} \begin{bmatrix} 1 \\ 0 \\ 0 \end{bmatrix} = \begin{bmatrix} \cos\Phi \\ \sin\Phi \\ 0 \end{bmatrix}. \tag{2}$$

If the rotor plane is also tilted—taken to be a rotation by the angle δ about the y'-axis—then the normal vector to the rotor plane becomes

$$\hat{\boldsymbol{x}} = \begin{bmatrix} \cos\delta & 0 & \sin\delta \\ 0 & 1 & 0 \\ -\sin\delta & 0 & \cos\delta \end{bmatrix} \begin{bmatrix} \cos\Phi \\ \sin\Phi \\ 0 \end{bmatrix} = \begin{bmatrix} \cos\Phi\cos\delta \\ \sin\Phi \\ -\cos\Phi\sin\delta \end{bmatrix}. \tag{3}$$

With the wind vector at the actuator disk denoted $\boldsymbol{V} = [u\ v\ w]^{\mathrm{T}}$, the freestream wind speed to be used in BEM theory is given by

$$V_0 = \boldsymbol{V} \cdot \hat{\boldsymbol{x}} = u\cos\Phi\cos\delta + v\sin\Phi - w\cos\Phi\sin\delta. \tag{4}$$

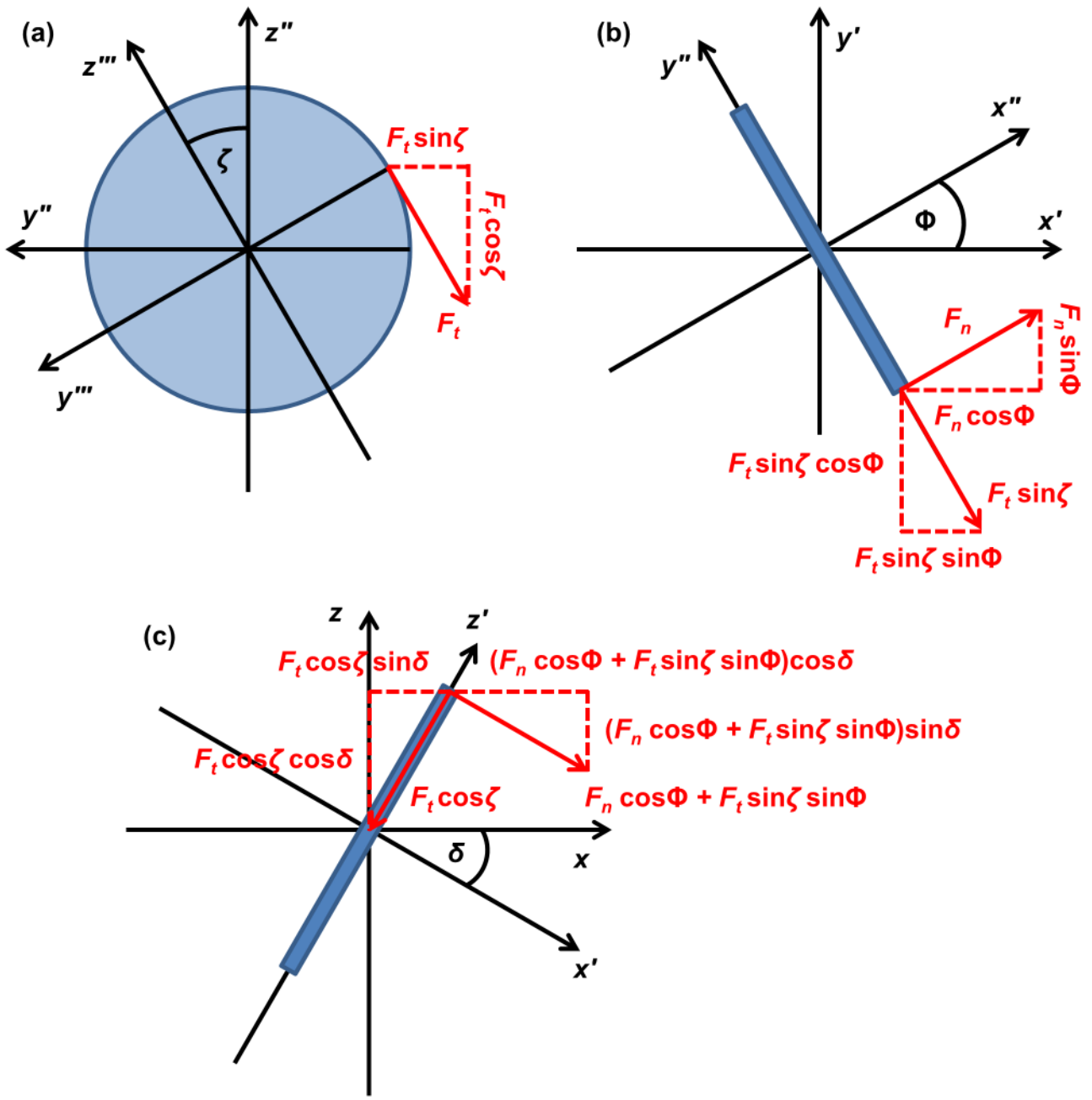

FIG. 2. Diagram of the coordinate system convention and components of the force acting on the actuator disk. Axes and angles are shown in black, forces in red, and the disk in blue. (a) The view upwind of the rotor along the longitudinal axis, (b) a bird's-eye view looking down at the rotor along the vertical axis, and (c) a side view of the rotor along the transverse axis.

Now, in the case of no rotor tilt, the components of the force $\boldsymbol{F}$ exerted on the actuator disk by the flow were found in Equations (A20–A22) of Mirocha et al. (2014) by applying successive rotations, one by the angle $-\zeta$ about the x''-axis and another by the angle Φ about the z''-axis:

$$\boldsymbol{F} = \begin{bmatrix} \cos\Phi & -\sin\Phi & 0 \\ \sin\Phi & \cos\Phi & 0 \\ 0 & 0 & 1 \end{bmatrix} \begin{bmatrix} 1 & 0 & 0 \\ 0 & \cos\zeta & \sin\zeta \\ 0 & -\sin\zeta & \cos\zeta \end{bmatrix} \begin{bmatrix} F_n \\ 0 \\ -F_t \end{bmatrix} = \begin{bmatrix} F_n\cos\Phi + F_t\sin\zeta\sin\Phi \\ F_n\sin\Phi - F_t\sin\zeta\cos\Phi \\ -F_t\cos\zeta \end{bmatrix}, \tag{5}$$

where F_n and F_t are the normal and tangential forces, respectively, acting at a point on the disk. In the case of nonzero rotor tilt, on the other hand, a third rotation by the angle δ about the y'-axis must be applied to the vector in Equation (5):

$$\boldsymbol{F} = \begin{bmatrix} \cos\delta & 0 & \sin\delta \\ 0 & 1 & 0 \\ -\sin\delta & 0 & \cos\delta \end{bmatrix} \begin{bmatrix} F_n\cos\Phi + F_t\sin\zeta\sin\Phi \\ F_n\sin\Phi - F_t\sin\zeta\cos\Phi \\ -F_t\cos\zeta \end{bmatrix} \tag{6}$$

$$= \begin{bmatrix} F_n\cos\Phi\cos\delta + F_t\sin\zeta\sin\Phi\cos\delta - \mathrm{F_t}\cos\zeta\sin\delta \\ F_n\sin\Phi - F_t\sin\zeta\cos\Phi \\ -F_n\cos\Phi\sin\delta - F_t\sin\zeta\sin\Phi\sin\delta - \mathrm{F_t}\cos\zeta\cos\delta \end{bmatrix}$$

Simulations were performed after incorporating the above modifications and results are presented below.

III. RESULTS

Prior to verifying the simulated wake characteristics, the WRF-LES inflow must first be compared to the observations. Statistics for the simulated inflow were gathered by sampling the hub height wind speed and direction over the course of the 5-hour run at a point located 2.5D upwind of the turbine, which corresponds to the recommended distance for measuring freestream winds in the determination of wind turbine power performance (International Electrotechnical Commission 2005). As seen in the histograms in Fig. 3, the wind speed varies over a range of 4 to 8 m s^{-1} with an average of 6.4 m s^{-1}, and almost all of the wind direction values are contained within a 20° range about the predominant value of 270°, very closely matching the measured inflow conditions in both cases. Note that, as mentioned

previously, the computational setup was simplified by orienting the predominant inflow direction at hub height to be parallel to the *x*-axis, such that individual simulated wind direction values are not meant to match their measured counterparts. The relative wind direction *ranges*, however, are in very good agreement, as intended.

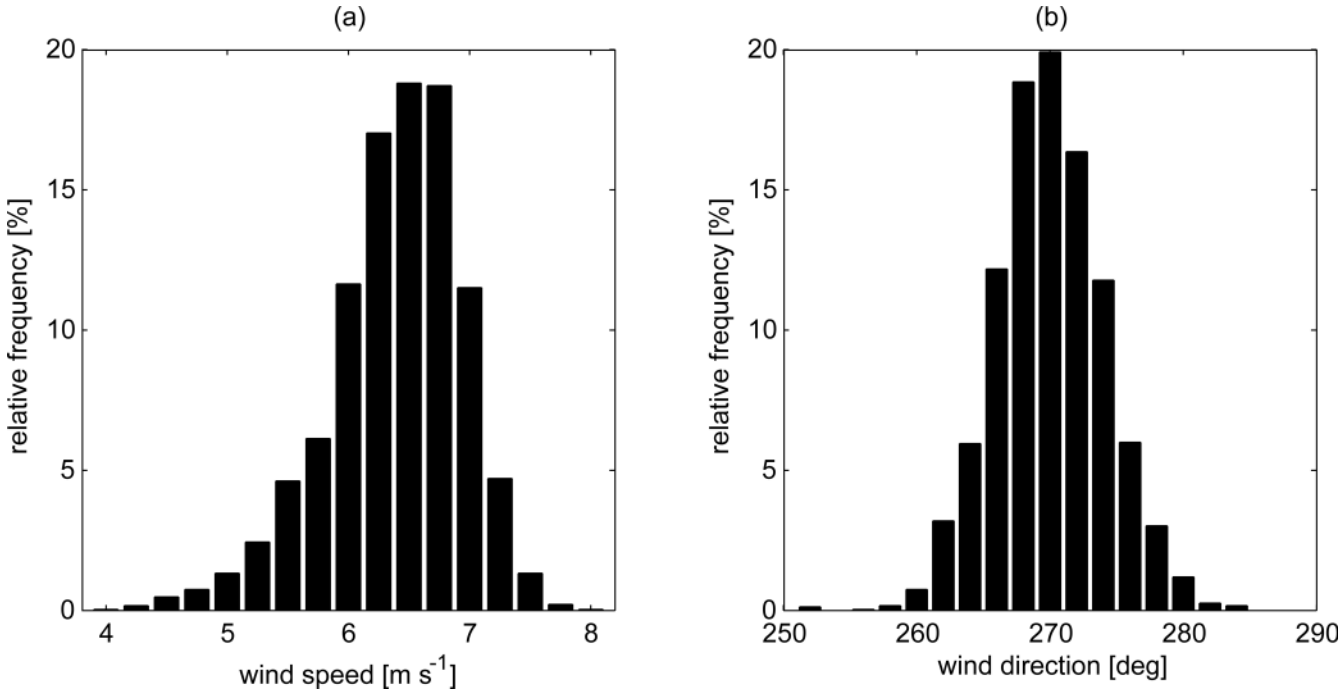

FIG. 3. Histograms of the simulated hub height (a) wind speed and (b) direction at a point located 2.5D upwind of the turbine.

The instantaneous contours of wind speed in Fig. 4 indicate the turbulent nature of the both the background flow field and the wake itself. Close to the turbine, the wake is relatively coherent and the wind speeds inside the wake are noticeably smaller than in the surrounding flow. Farther downwind, on the other hand, the wake is more diffuse and the wind speeds inside the wake are comparable to that of lulls in the ambient flow. Moreover, meandering behavior is apparent in the far wake region of Fig. 4a as ambient turbulence causes the wake to move randomly about the prevailing wind direction.

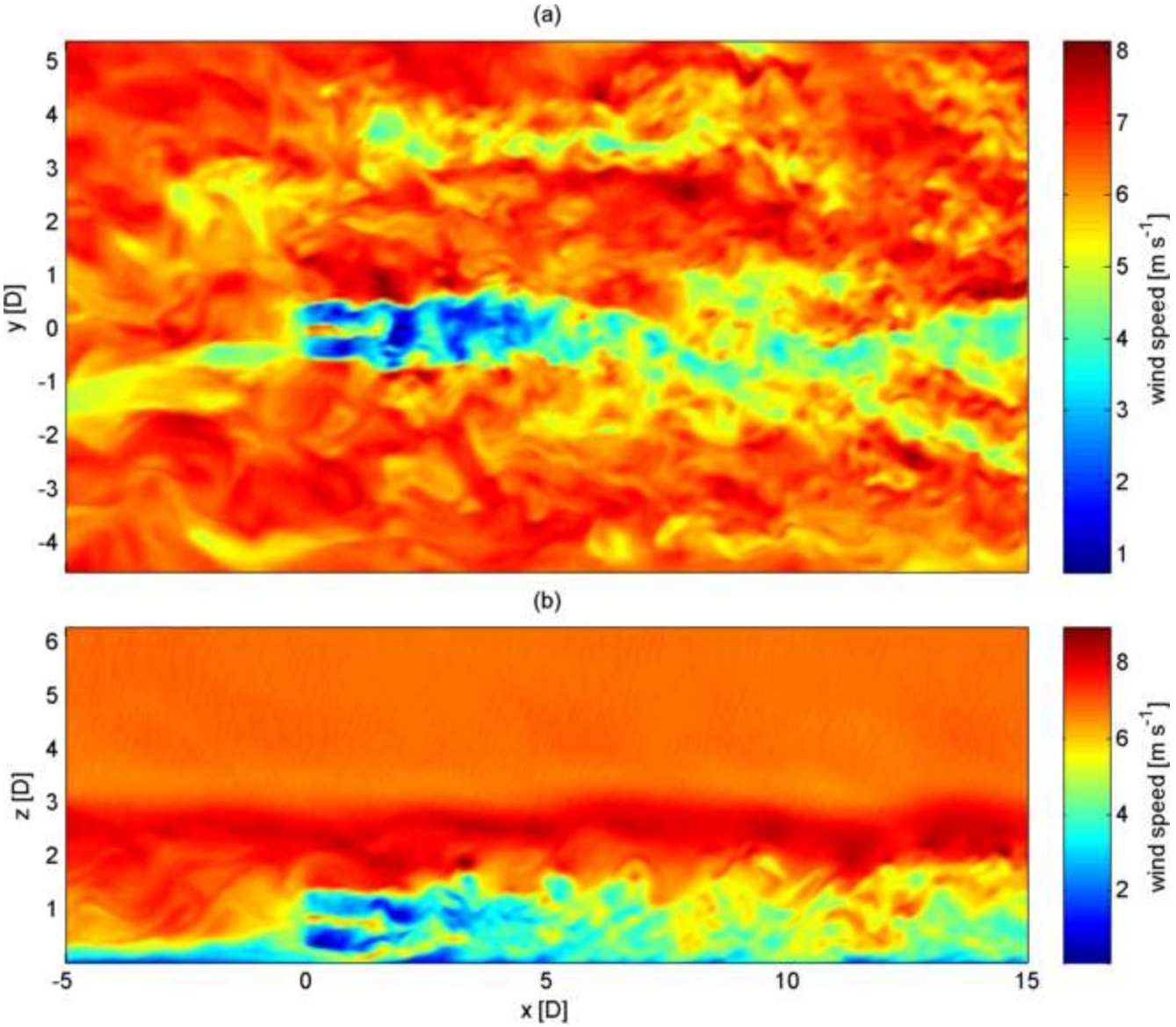

FIG. 4. Instantaneous contours of wind speed in the (a) *x*-*y* plane and (b) *x*-*z* plane at the center of the disk at hour 12 in the simulation. The turbine is located at $x = y = 0$.

To enable the comparison between computational and experimental results, we adopted the procedure outlined in Aitken and Lundquist (2014) for quantifying wake characteristics, in which unknown parameters in a nonlinear statistical model are estimated using successive wind speed profiles. The procedure is justified when the residuals are independent, which is certainly true in the real world where various forcings—such as terrain features and obstacles, as well as heterogeneous land cover and

surface conditions—serve to break up correlations in the turbulence structure. In the case of the measured data, a model fit is made to each lidar scan, which can be thought of as a quasi-instantaneous representation of the flow. On the other hand, the idealized setup in the simulations includes flat terrain along with uniform forcing at the surface and in the geostrophic wind, leading the turbulence structure to contain more robust correlations than would otherwise occur in nature. As a result, the wake detection algorithm cannot be applied to the instantaneous WRF-LES output in this case, or else the estimated wake parameters would be biased, and—more concerning—the model could potentially mistake a lull in the ambient flow for a wake. To avoid these issues, the WRF-LES output is first averaged in time before performing the model fit. The wake detection procedure will be applied to instantaneous WRF-LES output in future simulations that incorporate terrain and more realistic boundary conditions, facilitating the comparison between measured and simulated results.

With these caveats in mind, a comparison of the velocity deficit (VD) as a function of downwind distance x is shown in Fig. 5a. The blue central line depicts the median measured value, and the shaded region indicates one standard deviation on either side. The red line, on the other hand, indicates VD values computed from the mean LES field. Moreover, a comparison of the wake width w vs. x is shown in Fig. 5b, which shares the same color scheme as Fig. 5a. In the case of the velocity deficit, the simulation results are within the uncertainty in the experiment. The simulated wake width is also in good agreement with the measurements, aside from the two range gates at x = 2.4D and x = 3D. Compared to the wake width measurements taken over the entire field campaign (Aitken and Lundquist 2014), the average wake width estimates at these two range gates were unusually high for the 5-hour period considered here, which could be related to the small sample size of the case study. Given the constraints in both the experiment and the simulation—including 4-min lidar scans, a limited sample size, and an idealized simulation setup—the actuator disk model in WRF-LES adequately reproduces the measured

wake characteristics. We expect to see even closer agreement in future work by making use of higher resolution lidar data and more realistic simulations.

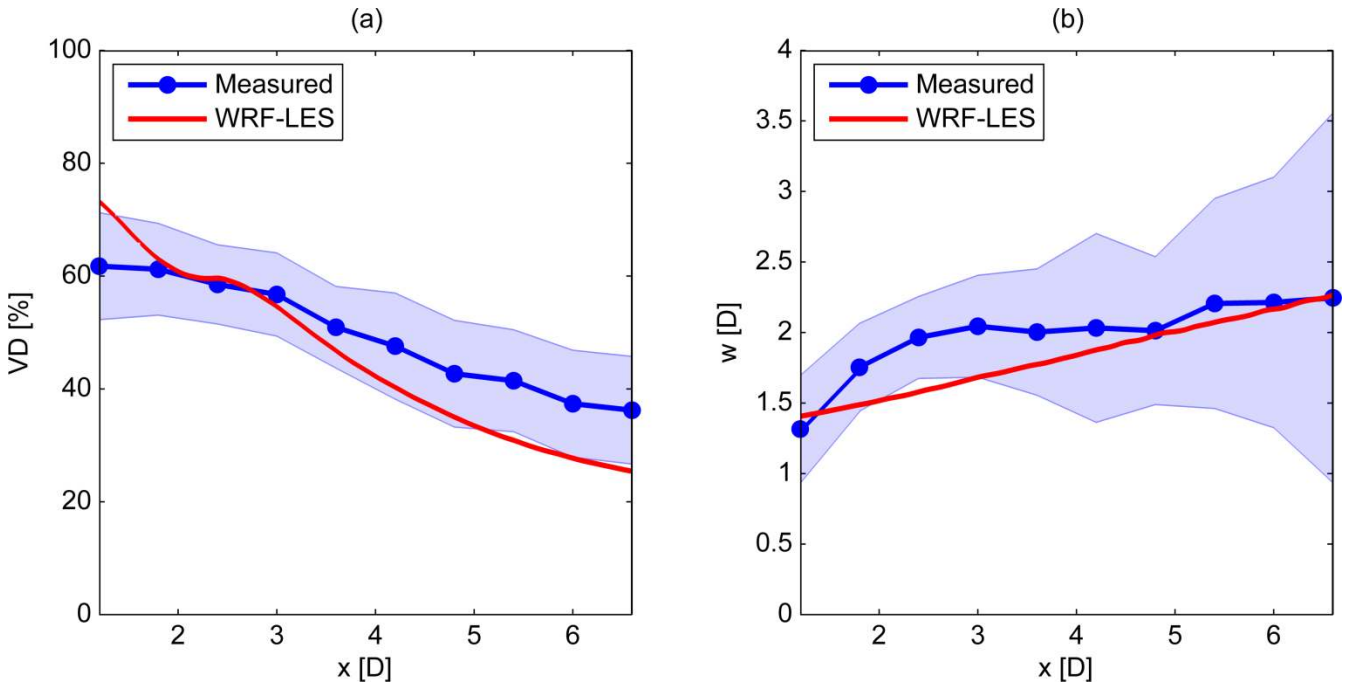

FIG. 5. (a) Velocity deficit and (b) wake width versus downwind distance. In each subplot, the blue central lines indicate median measured values, whereas the symmetric shaded error bars represent the standard deviation of the measurements. Simulation results are plotted in red.

Now, in the near wake—within a few rotor diameters downstream of the turbine—the velocity deficit profile is expected to have a double-Gaussian shape, i.e., the profile contains two local minima corresponding to the points of maximum lift along the blades. On the other hand, in the far wake, turbulent mixing causes the two troughs from the near wake to merge and form a single local minimum, and the profile is Gaussian in shape (Magnusson 1999; Aitken et al. 2014; Aitken and Lundquist 2014). Fig. 6 shows, as a function of x, the percentage of scans for which a wake was determined from the measured data to be statistically significant in comparison to the background flow. The total number of detected wakes increases from x = 1.8D to x = 3D as the lidar field-of-view increases, allowing a wider portion of the flow to be captured in the scan. However, wakes are detected with diminishing frequency

after x = 3D because (1) the amplitude of the velocity deficit decreases and therefore scales increasingly with the variability in the ambient flow and (2) velocity measurements become less precise, with lidar SNR falling off as $1/r^2$ (Fujii and Fukuchi 2005). As expected, a large fraction of the wakes were seen to have a double-Gaussian velocity deficit profile close to the turbine, and hardly any double-Gaussian wakes were detected after x = 3D, which may be considered the division between the near and far wake. Interestingly, x = 3D is the same distance at which the average simulated flow field transitions from a double-Gaussian to a single-Gaussian velocity deficit profile, indicating that the actuator disk model in WRF-LES is also capable of representing a realistic progression from the near wake to the far wake.

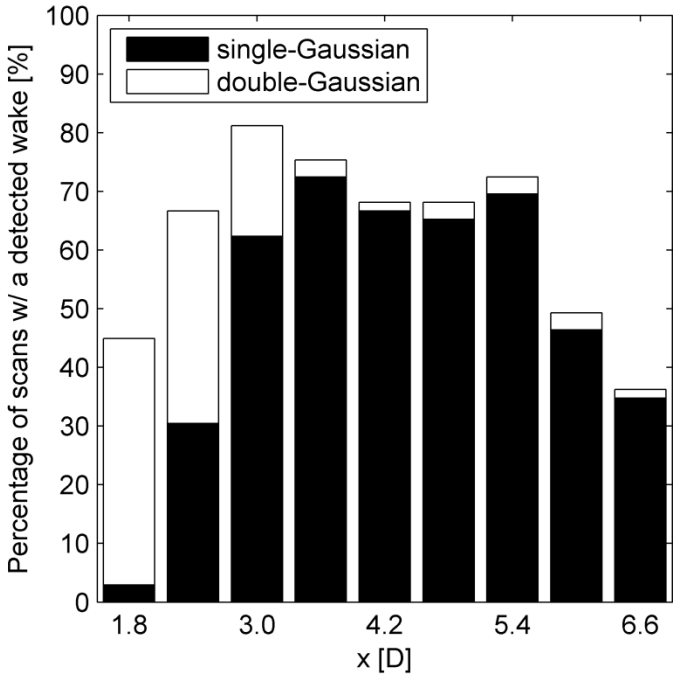

FIG. 6. Percentage of wakes detected from the measured data versus downwind distance.

One of the new contributions to the turbine model in WRF-LES is the inclusion of rotor tilt, which affects the vertical location of the wake centerline z_c, defined to be the height at which the velocity deficit inside the wake is maximum. The evolution of this parameter, which was determined using the

vertical scan (or RHI) algorithm from Aitken et al. (2014), appears in Fig. 7 as simulated both with and without rotor tilt. With the rotor thought of as an actuator disk, the net force on the flow by the turbine has a small component in the +z-direction when the rotor is tilted away from vertical (see Fig. 2c, noting that the force on the flow is equal to and opposite that on the disk), resulting in an upward shift of the wake center comparable to the horizontal displacement of the wake in the case of yawed flow. This upward shift is similar to that measured in Fig. 26 of Aitken et al. (2014).

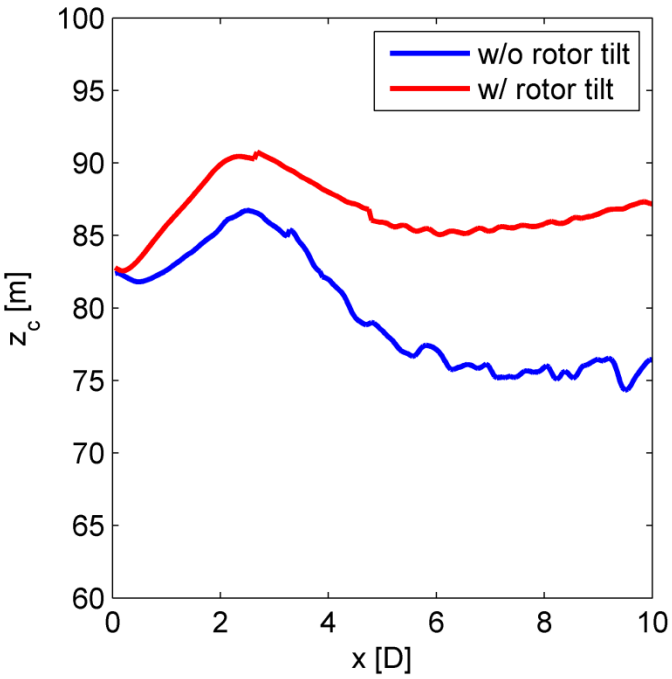

FIG. 7. Vertical location of the wake centerline versus downwind distance for simulations with and without rotor tilt.

IV. CONCLUSION

New features—namely rotor tilt and drag from the nacelle and tower—have been added to the actuator disk model in WRF-LES developed by Mirocha et al. (2014). To expand upon the convective case study in Mirocha et al. (2014), numerical simulations with this extension of the model were compared to nacelle-based scanning lidar measurements taken in stable atmospheric conditions. Using

the velocity deficit and wake width as metrics for model verification, the simulations show good agreement with the observations. Notable results include a high average velocity deficit, decreasing from 73% at x = 1.2D to 25% at x = 6.6D, resulting from a low average wind speed and therefore high average turbine thrust coefficient, in addition to the low background turbulence characteristic of stable conditions. Moreover, the wake width was seen to expand from 1.4D at x = 1.2D to 2.3D at x = 6.6D. Compared to the rotor, the effect of the tower and nacelle on the flow is relatively small but nevertheless important for an accurate representation of the entire wake. The inclusion of rotor tilt in the model causes the vertical location of the wake center to shift upward, which has important implications for the design of turbine layouts and controls at wind farms.

Further verification of the actuator disk model in WRF-LES will require that simulations of various types of turbines and atmospheric conditions be evaluated against corresponding experimental data. In addition to comparison with wake observations aloft, LES results should also be compared to the measured effects of turbines on wind speed, turbulence, and temperature at the surface (Rajewski et al. 2013). An interesting extension of the stable boundary layer case presented here would be to simulate a turbine operating in a low-level jet (Blackadar 1957; Bonner 1968; Banta et al. 2002; Lundquist and Mirocha 2008). Moreover, future simulations ought to incorporate both terrain features and more realistic inflow from mesoscale models to better represent turbulence. Several turbulence closure schemes—such as the dynamic reconstruction model (Chow et al. 2005) and the locally averaged scale-dependent dynamic model (Basu and Porté-Agel 2006)—should be tested under various atmospheric conditions to determine the most appropriate model for each scenario. Using the actuator disk model developed in Mirocha et al. (2014) and expanded upon here, more detailed features may be added, such as the blade coning angle (Mikkelsen 2003). Once computing resources allow WRF-LES to be run at sufficiently high resolution, actuator line techniques (Mikkelsen 2003; Churchfield et al. 2012) may

eventually be implemented to supplant the actuator disk model considered here. Still, there are many practical applications for the current framework in the meantime. For example, modeling an array of turbines within a single domain could be used to verify the mesoscale wind farm parameterization in WRF (Fitch et al. 2012) under changing stability conditions (Fitch et al. 2013). Furthermore, the actuator disk model could be used to study optimal turbine configurations within wind farms, as in Meyers and Meneveau (2012) and Archer et al. (2013), helping to minimize wake effects and thus the cost of energy.

ACKNOWLEDGMENTS

We wish to thank the wind farm operator for generously collecting and sharing the observational data and for providing the wind turbine specifications used in the actuator disk model. Many thanks also to Brian Vanderwende for innumerable helpful discussions on WRF and high performance computing. This work utilized the Janus supercomputer, which is supported by the National Science Foundation (award number CNS-0821794), the University of Colorado Boulder, the University of Colorado Denver, and the National Center for Atmospheric Research. The Janus supercomputer is operated by the University of Colorado Boulder. Parts of this research were supported by the National Renewable Energy Laboratory under Prof. Lundquist's Joint Appointment, UGA-0-41026-22 and UGA-0-41026-65.

REFERENCES

Aitken, M. L., M. E. Rhodes, and J. K. Lundquist, "Performance of a wind-profiling lidar in the region of wind turbine rotor disks," J. Atmos. Ocean. Tech. **29**, 347–355 (2012).

Aitken, M. L., R. M. Banta, Y. L. Pichugina, and J. K. Lundquist, "Quantifying wind turbine wake characteristics from scanning remote sensor data," J. Atmos. Ocean. Tech. doi:10.1175/JTECH-D-13-00104.1, in press (2014).

Aitken, M. L., and J. K. Lundquist, "Utility-scale wind turbine wake characterization using nacelle-based long-range scanning lidar," J. Atmos. Ocean. Tech., in review (2014).

Archer, C. L., S. Mirzaeisefat, and S. Lee, "Quantifying the sensitivity of wind farm performance to array layout options using large-eddy simulation," Geophys. Res. Lett. **40**, 4963–4970 (2013).

Banta, R. M., R. K. Newsom, J. K. Lundquist, Y. L. Pichugina, R. L. Coulter, and L. Mahrt, "Nocturnal low-level jet characteristics over Kansas during CASES-99," Bound.-Lay. Meteorol. **105**, 221–252 (2002).

Barthelmie, R. J., and L. E. Jensen, "Evaluation of wind farm efficiency and wind turbine wakes at the Nysted offshore wind farm," Wind Energy **13**, 573–586 (2010).

Basu, S., and F. Porté-Agel, "Large-eddy simulation of stably stratified atmospheric boundary layer turbulence: a scale-dependent dynamic modeling approach," J. Atmos. Sci. **63**, 2074–2091 (2006).

Basu, S., A. A. M. Holtslag, B. J. H. Van de Wiel, A. F. Moene, and G.-J. Steeneveld, "An inconvenient 'truth' about using sensible heat flux as a surface boundary condition in models under stably stratified regimes," Acta Geophys. **56**, 88–99 (2008).

Blackadar, A. K., "Boundary layer wind maxima and their significance for the growth of nocturnal inversions," B. Am. Meteorol. Soc. **38**, 283–290 (1957).

Blumen, W., R. Banta, S. P. Burns, D. C. Fritts, R. Newsom, G. S. Poulos, and J. Sun, "Turbulence statistics of a Kelvin-Helmholtz billow event observed in the night-time boundary layer during the Cooperative Atmosphere-Surface Exchange Study field program," Dynam. Atmos. Oceans **34**, 189–204 (2001).

Bonner, W. D., "Climatology of the low level jet," Mon. Wea. Rev. **96**, 833–850 (1968).

Chow, F. K., R. L. Street, M. Xue, and J. H. Ferziger, "Explicit filtering and reconstruction turbulence modeling for large-eddy simulation of neutral boundary layer flow," J. Atmos. Sci. **62**, 2058–2077 (2005).

Churchfield, M. J., S. Lee, J. Michalakes, and P. J. Moriarty, "A numerical study of the effects of atmospheric and wake turbulence on wind turbine dynamics," J. Turbul. **13**, 1–32 (2012).

El Kasmi, A., and C. Masson, "An extended k-ε model for turbulent flow through horizontal-axis wind turbines," J. Wind Eng. Ind. Aerod. **96**, 103–122 (2008).

Fitch, A. C., J. B. Olson, J. K. Lundquist, J. Dudhia, A. K. Gupta, J. Michalakes, and I. Barstad, "Local and mesoscale impacts of wind farms as parameterized in a mesoscale NWP model," Mon. Wea. Rev. **140**, 3017–3038 (2012).

Fitch, A. C., J. K. Lundquist, and J. B. Olson, "Mesoscale influences of wind farms throughout a diurnal cycle," Mon. Weather Rev. **141**, 2173–2198 (2013).

Fujii, T., and T. Fukuchi, *Laser Remote Sensing* (Taylor & Francis Group, Boca Raton, FL, 2005).

Hansen, K. S., R. J. Barthelmie, L. E. Jensen, and A. Sommer, "The impact of turbulence intensity and atmospheric stability on power deficits due to wind turbine wakes at Horns Rev wind farm," Wind Energy **15**, 183–196 (2012).

International Electrotechnical Commission, "Wind turbines—Part 12-1: Power performance measurements of electricity producing wind turbines," IEC 61400-12-1 International Standard (2005).

Kelley, N. D., B. J. Jonkman, and G. N. Scott, "The Great Plains turbulence environment: its origins, impact and simulation," National Renewable Energy Laboratory Conference Paper, NREL/CP-500-40176 (2006).

Kosović, B., "Subgrid-scale modelling for the large-eddy simulation of high-Reynolds-number boundary layers," J. Fluid Mech. **336**, 151–182 (1997).

Kosović, B., and J. A. Curry, "A large eddy simulation study of a quasi-steady, stably stratified atmospheric boundary layer," J. Atmos. Sci. **57**, 1052–1068 (2000).

Lundquist, J. K., and J. D. Mirocha, "Interaction of nocturnal low-level jets with urban geometries as seen in Joint Urban 2003 data," J. Appl. Meteorol. Clim. **47**, 44–58 (2008).

Magnusson, M., "Near-wake behavior of wind turbines," J. Wind Eng. Ind. Aerod. **80**, 147–167 (1999).

Mahrt, L., "Stably stratified atmospheric boundary layers," Annu. Rev. Fluid Mech. **46**, 23–45 (2014).

Meyers, J., and C. Meneveau, "Optimal turbine spacing in fully developed wind farm boundary layers," Wind Energy **15**, 305–317 (2012).

Mikkelsen, R., Ph.D. dissertation, Technical University of Denmark, 2003.

Mirocha, J. D., J. K. Lundquist, and B. Kosović, "Implementation of a nonlinear subfilter turbulence stress model for large-eddy simulation in the Advanced Research WRF Model. Mon. Weather Rev. **138**, 4212–4228 (2010).

Mirocha, J. D., B. Kosović, M. L. Aitken, and J. K. Lundquist, "Implementation of a generalized actuator disk wind turbine model into the Weather Research and Forecasting Model for large-eddy simulation applications," J. Renew. Sust. Energ. **6**, 013104-1–013104-19 (2014).

Park, J., S. Basu, and L. Manuel, "Large-eddy simulation of stable boundary layer turbulence and estimation of associated wind turbine loads," Wind Energy **17**, 359–384 (2014).

Rajewski, D. A., E. S. Takle, J. K. Lundquist, S. Oncley, J. H. Prueger, T. W. Horst, M. E. Rhodes, R. Pfeiffer, J. L. Hatfield, K. K. Spoth, and R. K. Doorenbos, "Crop Wind Energy Experiment (CWEX):

observations of surface-layer, boundary layer, and mesoscale interactions with a wind farm," Bull. Amer. Meteor. Soc. **94**, 655–672 (2013).

Saiki, E., C. Moeng, and P. Sullivan, "Large-eddy simulation of the stably stratified planetary boundary layer," Bound.-Lay. Meteorol. **95**, 1–30 (2000).

Sathe, A., J. Mann, T. Barlas, W. A. A. M. Bierbooms, and G. J. W. van Bussel, "Influence of atmospheric stability on wind turbine loads," Wind Energy **16**, 1013–1032 (2013).

Scamarock, W. C., J. B. Klemp, J. Dudhia, D. O. Gill, D. M. Barker, M. G. Duda, X.-Y. Huang, W. Wang, and J. G. Powers, "A description of the advanced research WRF version 3," National Center for Atmospheric Research Technical Note, NCAR/TN-475+STR (2008).

Smalikho, I. N., V. A. Banakh, Y. L. Pichugina, W. A. Brewer, R. M. Banta, J. K. Lundquist, and N. D. Kelley, "Lidar investigation of atmosphere effect on a wind turbine wake," J. Atmos. Ocean. Tech. **30**, 2554–2570 (2013).

Vanderwende, B. J., and J. K. Lundquist, "The modification of wind turbine performance by statistically distinct atmospheric regimes," Environ. Res. Lett. **7**, 034035-1–034035-7 (2012).

Vermeer, L. J., J. N. Sørensen, and A. Crespo, "Wind turbine wake aerodynamics," Prog. Aerosp. Sci. **39**, 467–510 (2003).

Wagner, R., I. Antoniou, S. M. Pedersen, M. S. Courtney, and H. E. Jørgensen, "The influence of the wind speed profile on wind turbine performance measurements," Wind Energy **12**, 348–362 (2009).

Wharton, S., and J. K. Lundquist, "Atmospheric stability affects wind turbine power collection," Environ. Res. Lett. **7**, 014005-1–014005-9 (2012)

Wu, Y.-T., and F. Porté-Agel, "Large-eddy simulation of wind-turbine wakes: evaluation of turbine parametrisations," Bound.-Lay. Meteorol. **138**, 345–366 (2011).

Zhou, B., and F. K. Chow, "Large-eddy simulation of the stable boundary layer with explicit filtering and reconstruction turbulence modeling," J. Atmos. Sci. **68**, 2142–2155 (2011).